Effects of Combustor-Level High Inlet Turbulence on the Endwall Flow and Heat/Mass Transfer of a High-Turning Turbine Rotor Cascade

Sang Woo Lee*, Sang Bae Jun
School of Mechanical Engineering Kumoh National Institute of Technology
188 Shinpyong, Gumi, Gyongbook 730-701, Korea
Byung-Kyu Park, Joon Sik Lee
School of Mechanical and Aerospace Engineering Seoul National University
Seoul 151-742, Korea

Experimental data are presented which describe the effects of a combustor-level high free-stream turbulence on the near-wall flow structure and heat/mass transfer on the endwall of a linear high-turning turbine rotor cascade. The endwall flow structure is visualized by employing the partial- and total-coverage oil-film technique, and heat/mass transfer rate is measured by the naphthalene sublimation method. A turbulence generator is designed to provide a highly-turbulent flow which has free-stream turbulence intensity and integral length scale of 14.7% and 80mm, respectively, at the cascade entrance. The surface flow visualizations show that the high free-stream turbulence has little effect on the attachment line, but alters the separation line noticeably. Under high free-stream turbulence, the incoming near-wall flow upstream of the adjacent separation lines collides more obliquely with the suction surface. A weaker lift-up force arising from this more oblique collision results in the narrower suction-side corner vortex area in the high turbulence case. The high free-stream turbulence enhances the heat/mass transfer in the central area of the turbine passage, but only a slight augmentation is found in the endwall regions adjacent to the leading and trailing edges. Therefore, the high free-stream turbulence makes the endwall heat load more uniform. It is also observed that the heat/mass transfers along the locus of the pressure-side leg of the leading-edge horseshoe vortex and along the suction-side corner are influenced most strongly by the high free-stream turbulence. In this study, the endwall surface is classified into seven different regions based on the local heat/mass transfer distribution, and the effects of the high free-stream turbulence on the local heat/mass transfer in each region are discussed in detail.

Key Words : Gas Turbine, Turbine Rotor, Endwall, Combustor-Level Turbulence, Turbulence Intensity, Integral Length Scale, Near-Wall Flow, Heat/Mass Transfer

Nomenclature

b : Axial chord length, Fig. 2
c : Chord length, Fig. 2
C_p : Specific heat at constant-pressure
D : Diffusion coefficient of naphthalene in air
h_m : Local mass transfer coefficient
I : I-th measurement location in the x-direction, Fig. 4
J : J-th measurement location in the y-direction, Fig. 4
l : Pitchwise distance between the pre-

* Corresponding Author,
E-mail : swlee@kumoh.ac.kr
TEL : +82-54-467-4209; **FAX** : +82-54-467-4050
School of Mechanical Engineering Kumoh National Institute of Technology 188 Shinpyong, Gumi, Gyongbook 730-701, Korea. (Manuscript **Received** October 16, 2003; **Revised** May 18, 2004)

ssure and suction surfaces
L_∞ : Free-stream integral length scale
p : Pitch, Fig. 2
Pr : Prandtl number, v/α
Re_∞ : Inlet Reynolds number, $U_\infty c/v$
s : Span, Fig. 1
Sc : Schmidt number, v/D
St : Local heat transfer Stanton number, $h/(\rho C_p U_\infty)$
St_m : Local mass transfer Stanton number, h_m/U_∞
$\overline{St}_m$: Mass transfer Stanton number averaged in the y-direction
$(\overline{St}_m)_{av}$: Mass transfer Stanton number averaged across the whole measurement area
Tu_∞ : Free-stream turbulence intensity
U_∞ : Inlet free-stream velocity
w : Width of the inlet duct, Fig. 1
x_D, y_D, z_D : Coordinates at the inlet duct, Fig. 1
x, y, z : Cascade coordinates, Fig. 2
y_s : Distance in the y-direction from the suction surface

Greek Characters

α : Thermal diffusivity of air
β_1 : Blade inlet angle, Fig. 2
β_2 : Blade outlet angle, Fig. 2
δ_2 : Displacement thickness
δ_{99} : Boundary-layer thickness
δ^* : Momentum thickness
v : Kinematic viscosity of air
ρ : Density of air

1. Introduction

For the advances in gas turbine performance, turbine durability problems due to hot gas temperature should be resolved. Higher turbine inlet temperature generally causes increased metal temperature and steeper temperature gradient in the turbine hot components such as a blade and an endwall. Recent combustor design, which aims reduced emissions, provides higher gas temperature near the endwall with a flattened temperature distribution (Oke et al., 2000). The endwall thus needs a sophisticated cooling scheme as found in turbine blade cooling.

The endwall as well as the turbine blade is exposed to very high inlet free-stream turbulence with a large length scale. Turbulence measurements taken at the exit of various gas turbine combustors have shown that the level can range between 8 percent and 40 percent (Goldstein et al., 1983; Koutmos and McGuirk, 1989; Goebel et al., 1993), which may have a certain effect on the endwall heat transfer. In order to design an efficient cooling configuration for the turbine endwall, a detailed description of the heat transfer coefficient is essential.

One of the earliest studies on the endwall heat transfer is presented by Blair (1974), who conducted experiments to determine the film-cooling effectiveness and heat transfer coefficient on a simulated turbine vane endwall with a cooling slot injection. Graziani et al.(1980) measured local Stanton numbers on an electrically-heated turbine endwall and blade surface for two different inlet boundary layer thicknesses. They found that the endwall heat transfer is affected strongly by the passage vortex, and the inlet boundary-layer thickness on the endwall has a significant effect on the endwall and suction surface heat transfer. According to Gaugler and Russell (1984), there is an obvious correlation between the visualized secondary flow and measured endwall Stanton-number distribution near a vane cascade entrance, but the effect of the secondary flow is not obvious in the passage. York et al. (1984) measured local Stanton numbers on a vane endwall with thermocouples for different Mach and Reynolds numbers. However, their data could not explain heat transfer characteristics in relation to secondary flows. In the measurement of the endwall heat transfer, Goldstein and Spores (1988) employed the naphthalene sublimation technique, and provided much detailed distributions of the local endwall transport coefficient for a turbine rotor cascade by eliminating a conduction error in the conventional heat transfer instrumentation. At a low turbulence level of about 1.2 percent, they investigated the effects of Reynolds number and inlet boundary layer thickness. More recently, Kang et al.(1999) and Kang and Thole (2000) showed through

endwall heat transfer measurements for a first-stage vane cascade with an infrared thermography that the peak heat transfer coefficient occurs coincidentally at the downward legs of both the horseshoe vortex and passage vortex. They had a major focus on the heat transfer in the leading edge region and on the low free-stream turbulence cases. Even in the low turbulence cases, unfortunately, there are noticeable discrepancies among the recent endwall results such as by Kang et al.(1999) for a stator vane, by Goldstein and Spores (1988) and by Giel et al.(1998) for a turbine rotor blade.

Other recent work addressed high free-stream turbulence effects on the endwall heat transfer. Spencer et al.(1996) investigated the endwall heat transfer in an annular vane cascade at a free-stream turbulence level of 9 percent by employing a transient liquid crystal technique, but did not provide a comparison with corresponding low-turbulence data. Giel et al.(1998) measured local endwall heat transfer coefficients for a transonic rotor cascade using a steady-state liquid crystal technique at low and elevated turbulence intensities of 0.25 and 7.0 percent. They reported somewhat surprising results that the primary effect of the elevated turbulence intensity is to lower peak heat transfer level particularly at the entrance of the cascade passage. It was also shown that the elevated turbulence has essentially no effect on the heat transfer downstream of the cascade. Radomsky and Thole (2000) firstly measured the endwall heat transfer under a combustor-level high turbulence intensity of 19.5 percent for the same vane cascade as Kang et al.(1999) used. Their results show that the high turbulence enhances the endwall heat transfer, but the augmentations are either small or nonexistent in the leading-edge region and near the suction side of the blade. As in the low turbulence cases, an obvious conflict has been found between the recent heat transfer results by Giel et al.(1998) and by Radomsky and Thole (2000) at high inlet free-stream turbulence conditions. It is thus very important to figure out the discrepancies on the effect of the high free-stream turbulence on the endwall transport phenomena through a different approach. In order to do this, it is essential to fully understand the incoming endwall boundary-layer separation and its effect on the behavior of the near-wall flow under the high free-stream turbulence.

In this study, the effects of combustor-level high free-stream turbulence with a large length scale on the endwall convective transport have been investigated for a high-turning turbine rotor cascade. The near-wall flow structure is presented including incoming boundary-layer separation by partial- and total-coverage oil-film endwall flow visualizations. The local transport coefficient is measured by the naphthalene sublimation technique so that a wall conduction error can safely be avoided.

2. Experimental Apparatus and Procedure

2.1 Naphthalene sublimation technique

In this technique, mass transfer coefficient, h_m, is evaluated from the corresponding sublimation depth of cast naphthalene. Mass transfer Stanton number, St_m, which is commonly used as dimensionless mass transfer coefficient, is defined as

$$St_m = \frac{h_m}{U_\infty} \tag{1}$$

Heat transfer Stanton number can be obtained in the following way, according to an analogy between heat and mass transfer (Goldstein and Cho, 1999).

$$\frac{St}{St_m} = \left(\frac{Pr}{Sc}\right)^{n-1} \tag{2}$$

where n is usually taken to be 1/3 for a laminar flow and to be 0.4 for a turbulent flow. The boundary condition in the heat transfer system is equivalent to the constant-temperature endwall.

2.2 Linear cascade wind tunnel

As shown in Fig. 1, the cascade wind tunnel comprises an open-circuit type wind tunnel, a high turbulence generator, an inlet duct, and a linear turbine cascade, and an exhaust section. The wind tunnel has a cross section of 0.6m × 0.4m, and the inlet duct has a cross section of

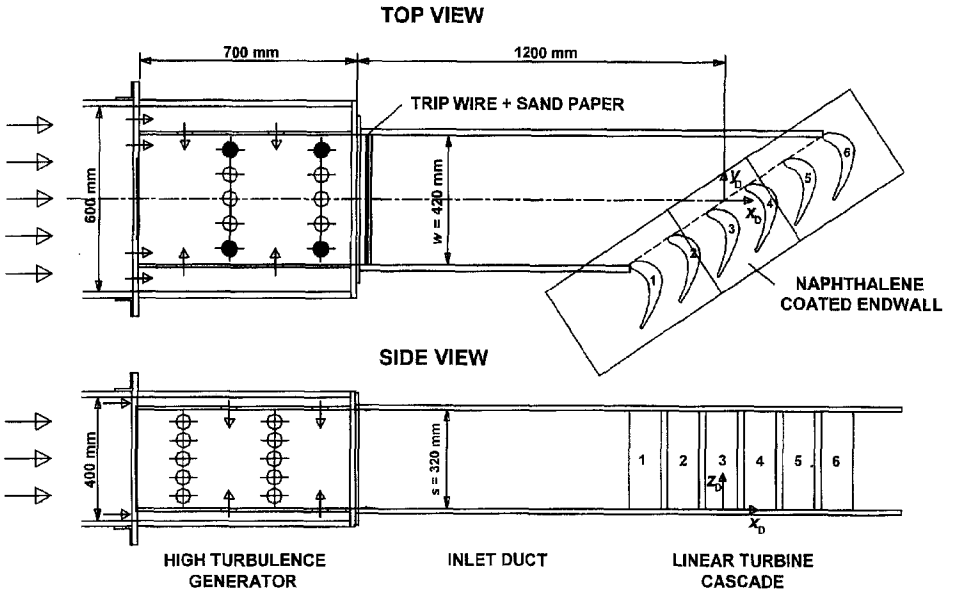

Fig. 1 Overall view of cascade wind tunnel

0.42m×0.32m. In the case necessary to generate low free-stream turbulence, the high turbulence generator is replaced with a three-dimensional contraction nozzle. The flow coming out from the contraction nozzle or the high turbulence generator is developing to a turbulent boundary-layer flow on the top and bottom walls of the inlet duct, after passing a trip wire and sand paper. The trip wire diameter is 1.8mm. As shown in Fig. 1, the linear turbine cascade has six turbine blades, and its entrance is located 1.20m downstream of the exit of the turbulence generator. The blades are fabricated based on the mid-span profile of a first-stage turbine rotor blade for power generation, and they are made of an engineering plastic (Ivory MC Nylon).

The coordinate origin is located on the endwall at the center of the central blade passage in the inlet plane of the cascade, and x_D, y_D, and z_D are streamwise, normal and spanwise coordinates with respect to the free-stream direction, respectively. In the xyz coordinates as shown in Fig. 2, x, y, and z are in the axial, pitchwise and spanwise directions of the cascade. As listed in Fig. 2, the chord length, c, axial chord, b, pitch, p, and span, s, are 217.8mm, 196.0mm, 151.6mm, and 320.0mm, respectively. The span is determined

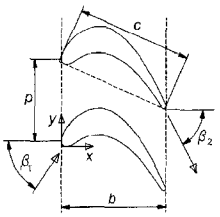

Number of blades	6
Chord length (c)	217.8 mm
Axial chord (b)	196.0 mm
Pitch (p)	151.6 mm
Span (s)	320.0 mm
Blade inlet angle (β_1)	56.4 deg
Blade outlet angle (β_2)	-62.6 deg

Fig. 2 Arrangement of turbine blade cascade

based on the span-to-chord ratio of the original rotor blade. The turning angle of the rotor blade is given as 119 degrees. The rotor blade profile used in this study is reported by Jun (2000).

2.3 High turbulence generator

As shown in Fig. 1 and Fig. 3, the high turbulence generator employed in this study is designed to simulate the highly turbulent flow from a combustor. In the previous work by Wang et al. (1999), their turbulence generator had only two side-plenums for jet injection. However, the present high turbulence generator has not only two side-plenums but also upper- and lower-plenums. Two rows of five injection holes of 50mm in diameter are drilled on the inside wall of each plenum. The inlet main passage of the high turbulence generator is blocked with an alumi-

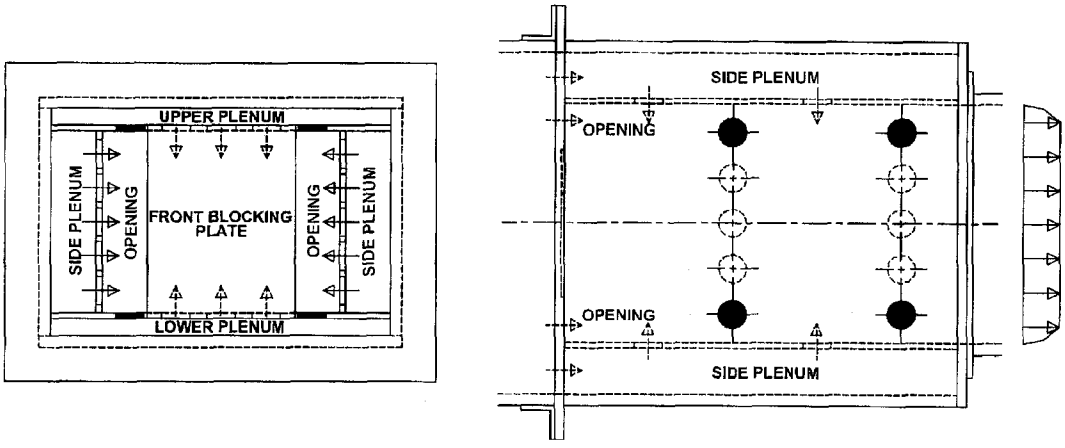

(a) Front view (b) Top view

Fig. 3 Detail of high turbulence generator

num plate as in Fig. 3(a), so that the approaching flow can enter easily into the four plenums. Jets issuing into the main passage through the injection holes interacts strongly with the mainflow from the two front openings, and produces very high turbulence. As the area of the front openings decreases, in general, the flow exiting the high turbulence generator tends to become more turbulent but less uniform. When jets are injected only from the side-plenums, a parabolic velocity distribution is obtained with the highest value at the mid-width of the inlet duct. This is because the opposing jets from the side plenums meet with each other at the mid-width. After some tests for various injection cases, the most uniform distribution with a relatively high turbulence value is finally obtained in the case that the jets are injected not only through the all twenty holes of the two side plenums but also through the central twelve holes of the upper and lower plenums. The shaded holes in Fig. 1 and Fig. 3 indicate those blocked with tape, so that no flow comes out through the shaded holes. In this situation, it is found that the injections from the upper and lower plenums effectively reduce the velocity surplus in the mid-width plane by blocking the mainflow, but tend to accelerate the side flows. Even though the boundary layer within the high turbulence generator is considerably disturbed by the jet injections from the upper and lower plenums, a new turbulent boundary layer flow is developed effectively after passing the trip wire and sand paper.

2.4 Naphthalene coated endwall

The endwall for the mass transfer measurement is shown in Fig. 4. A layer of naphthalene, which is 4mm thick, is cast on a grooved surface of the endwall with a well-polished mold made of aluminum. The cast endwall is installed in the turbine cascade as in Fig. 1. A very tiny hole is drilled on the metal shoulder of the endwall to

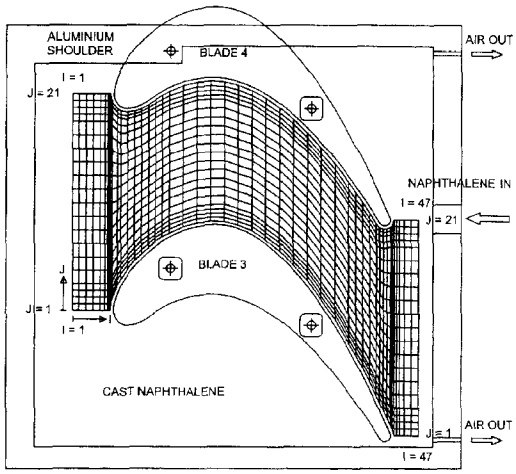

Fig. 4 Measurement locations on the naphthalene-cast endwall

provide a starting point of a depth gauge. A T-type thermocouple is embedded in the cast naphthalene to obtain the naphthalene surface temperature during the experiment. Sublimed depth are measured at 47 points in the x-direction and at 21 points in the y-direction. The grid in Fig. 4 indicates the measurement points. Considering the presence of the fillet along the original blade-endwall corner, the closest measurement locations are kept about 2mm apart from the corner line.

2.5 Data reduction systems

The measurements of the pressure, temperature, turbulence and naphthalene sublimation depth are controlled by a personal computer (IBM, AT 486) equipped with plug-in boards such as a Multi-Function DI/O Board (National Instruments, AT-MIO-16D-H-9) and a GPIB adapter (National Instruments, AT-GPIB). Measured pressures are transformed into DC voltages by a digital micro-monometer (Furness Controls, FCO12), and these signals are sampled by a 12-bit A-D converter in the Multi-Function DI/O Board, and then transferred to the computer. Temperatures of the free-stream and cast naphthalene are measured by T-type thermocouples connected to a digital voltmeter (Keithley, Model 2001TSCAN), which is controlled by the computer through the GPIB. Thermocouples are calibrated using a constant-temperature bath (Fisher Scientific, 9010) and a standard thermometer. Temperature measurements are based on the STP 470A (1974) published by ASTM. In the measurements of turbulence intensity and integral length scale, a constant-temperature hot-wire anemometer (Kanomax, model 1010) is used. The AC components of turbulence signal via a linearlizer (Kanomax, model 1013) are sampled at a rate of 50kHz after passing a 10kHz low-pass filter, and are then stored in a hard disk for the later evaluation of the auto-correlation function. The integral time scale is obtained by integrating the auto-correlation function, and then the integral length scale is evaluated from it with Taylor's hypothesis (Camp and Shin, 1995).

A LVDT (linear variable differential transformer) depth gauge (Sensortec, 060-3590-02) is used to measure the sublimation depth. Its full scale and resolution are $\pm$0.5mm and 0.5μm, respectively. In actual exposure experiments, the average sublimation depth is maintained approximately at 0.1mm, and maximum sublimation depth is less than about 0.3mm. When a smooth solid surface of naphthalene is obtained from the cast procedure, the test endwall is placed on a two-axis positioning system, which is equipped with linear motion guides (Samik, SAR1615T), stepping motors (Oriental Motor, UPH599-A), and stepping motor drivers (Oriental Motor, UDX5114). The first scanning of the naphthalene surface is conducted with the calibrated depth gauge at 987 locations as indicated in Fig. 4, before exposure to the air flow. It takes about 25 minutes to complete the total scanning. The readings of local elevation are recorded in the computer through the 12-bit A-D converter. Then, the endwall is positioned in the cascade. After it is exposed to the air flow for about 90 minutes, the endwall is brought back to the positioning system, and is scanned again. The difference between the before-and-after readings at each location still includes free-convection loss during the setup time of the cast endwall as well as during the depth measurements. This extra sublimation depth is typically about 2.5 percent of the average sublimation depth. The net sublimation depth, δz, is finally obtained after a proper correction.

2.6 Operating conditions and uncertainties

During the sublimation experiments, the free-stream velocity in the inlet duct is maintained at U_∞=20m/s at $x_D/c=-1.5$. An excellent pitchwise mean flow periodicity is obtained at the entrance of the central three blade-passages within 2 percent deviation. The inlet Reynolds number based on the free-stream velocity and the chord length, Re_∞, is 2.78×10^5. During exposure of the cast endwall to the cascade air flow, average naphthalene surface temperatures of the low and high turbulence experiments are 26.0℃ and 25.7℃, respectively, and their variations are kept within 0.2℃.

Table 1 Operating conditions at $x_D/c=-1.5$

	Free-Stream		Boundary Layer	
Low Turbulence Case	Re_∞	2.78×10^5	δ_{99}	44.7mm
	Tu_∞	1.2%	δ_2	5.16mm
	L_∞	—	δ^*	4.04mm
High Turbulence Case	Re_∞	2.78×10^5	δ_{99}	28.0mm
	Tu_∞	14.7%	δ_2	2.28mm
	L_∞	80mm	δ^*	1.92mm

In the low free-stream turbulence case, turbulence intensity is 1.2% at $x_D/c=-1.5$. At this location, the boundary-layer thickness, displacement thickness, and momentum thickness are 44.7mm, 5.16mm, and 4.04mm, respectively. In the case of the high free-stream turbulence, turbulence intensity and integral length scale are 14.7% and 80mm at $x_D/c=-1.5$, respectively, and the boundary-layer thickness, displacement thickness, and momentum thickness are 28.0mm, 2.28mm, and 1.92mm, respectively. The momentum thickness is less than a half of that in the low turbulence case. In general, the endwall heat transfer depends on the inlet momentum thickness. However, we do not attempt to make the momentum thicknesses the same in the two low and high turbulence cases, because the thinner momentum thickness is one of the major effects of the inlet high free-stream turbulence. The inlet flow conditions are summarized in Table 1.

In the low turbulence case, the measured values of the mass transfer Stanton number in the absence of the blades in the cascade are compared with those from a standard mass transfer correlation for the unheated starting length (Goldstein and Spores, 1988), which are calculated based on the extrapolated virtual origin. The comparison shows a good agreement within 3.4 percent between the two results. In addition, average mass transfer is augmented by about 6 percent, due solely to the thinner momentum thickness in the present high turbulence. The uncertainty interval of the mass transfer Stanton number with 95 percent confidence based on Abernethy et al. (1985) is estimated to be ±5.9 percent of St_m.

3. Results and Discussion

3.1 Endwall surface flow visualization

In the previous surface visualizations (Hudson and Dominy, 1987; Kang et al., 1999), it is not easy to identify the exact location of the separation line even in their low turbulence cases. In this study, for a precise identification of the separation line, two different approaches are employed in the oil-film method using a mixture of carbon black and kerosene (Lee et al., 1997). In the first approach (Method 1), only the upstream region 120mm ahead of the leading edges is initially coated with the oil film. In this method, the oil film flows with the incoming fluid in the downstream direction, so that the separation line can clearly be identified. In order to make the mixture move easily with the near-wall flow, kerosene is spread on the whole area of the endwall before partially coating the upstream region with the mixture. Contrary to this partial coverage, the whole endwall surface is initially covered with the oil film in the second approach (Method 2). Method 2 can provide a detail of flow traces in the whole endwall area, as by Hudson and Dominy (1987) and by Kang et al.(1999).

The endwall flow visualizations in the low turbulence case are shown in Figs. 5 and 6. The visualization in Fig 5, which is obtained by Method 1, clearly shows the separation of the incoming boundary-layer flow. The incoming flow, which drags the oil film into each turbine passage, is divided along each attachment line (line A_{L1}-A_{L2}) and then enters the corresponding passage between the adjacent attachment lines. The attachment line from the point A_{L1} to S_L is drawn based on the oil-film traces from both Method 1 and 2, but the line from the point S_L to A_{L2} is based on the traces only by Method 2. The line connecting the downstream edge of the region covered with the oil film (line B_{L1}-B_{L2}) is identified as a separation line. There exists no oil-film mixture in the region downstream of the separation line, because the oil film cannot lift off with the separated fluid due to the gravity. The inter section between the lines A_{L1}-A_{L2} and B_{L1}-B_{L2} is

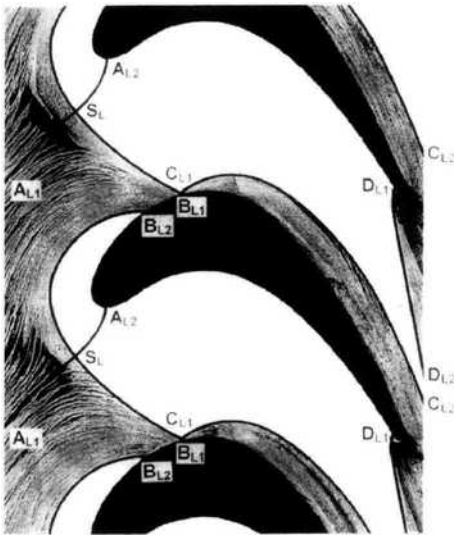

Fig. 5 Endwall surface flow visualization in Method 1 in the low turbulence case

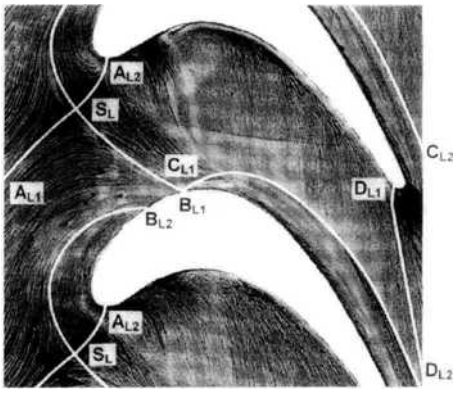

Fig. 6 Endwall surface flow visualization in Method 2 in the low turbulence case

called a saddle point (point S_L). The mixture approaching the cascade turns toward the suction surface in the region upstream of the adjacent separation lines, and then collides with it between the points B_{L1} and B_{L2}. Finally, the mixture climbs onto the suction surface, overcoming the gravity. Some of the mixture moves downstream along the suction surface with the aid of the upwash momentum of the passage vortex, while the remainder near the root of the suction surface is entrained into an endwall area where the suction-side corner vortex resides. This region is surrounded by the line C_{L1}-C_{L2}, as found along the suction-side corner as shown in Fig. 5. In this low turbulence case, the point B_{L1}, an endpoint of the separation line, is nearly identical to the point C_{L1}. The mixture moving downstream on the suction surface is separated from it at the trailing edge, and then touches the endwall region bounded by the line D_{L1}-D_{L2}. Figure 6 illustrates endwall flow structure which is obtained by superimposing the visualizations of Method 1 and 2. The white lines denote the superimposed ones. The oil-film traces in Fig. 6 clearly demonstrate the complicated near-wall flow patterns within the passage.

The endwall flow visualizations in the high turbulence case are shown in Figs. 7 and 8. Overall oil-film traces in Fig. 7 show similar near-wall flow features to those in Fig. 5. The region surrounded by the line C_{L1}-C_{L2} in Fig. 5 is considerably reduced in its area in Fig. 7. This implies that the suction-side corner vortex is weakened under high free-stream turbulence. In contrast to the location of the point C_{L1} in Fig. 5, the point C_{H1} in Fig. 7 does not coincide any more with the point B_{H1}, since due to less lift force on the mixture under high free-stream turbulence, some of the mixture cannot overcome the gravitational force and then it flows inevitably along the endwall between the points B_{H1} and C_{H1}. A

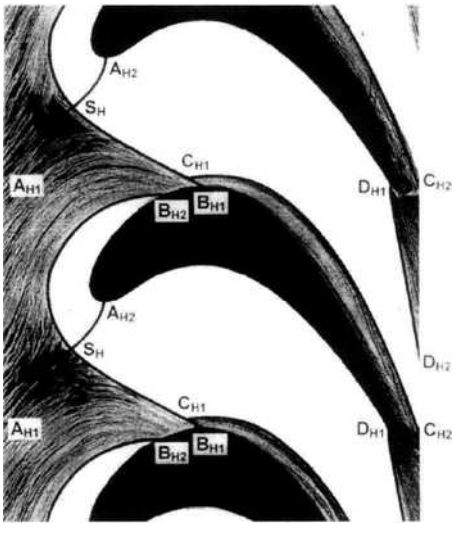

Fig. 7 Endwall surface flow visualization in Method 1 in the high turbulence case

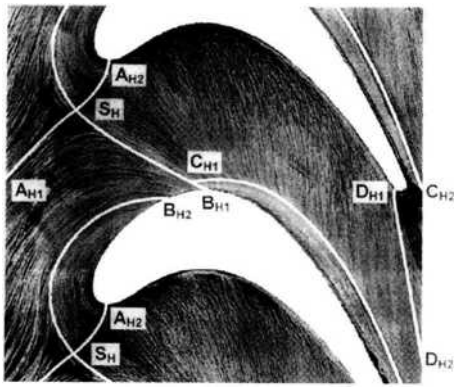

Fig. 8 Endwall surface flow visualization in Method 2 in the high turbulence case

close examination on the oil-film traces around the saddle point shows that the incoming oil film is accumulated about $0.05b$ ahead of the saddle point in the low turbulence case (Fig. 5), meanwhile the accumulation is found just ahead of the saddle point in the high turbulence case (Fig. 7). This means that the approaching flow near the endwall toward the saddle point has a higher velocity value under high turbulence than under low turbulence. This was also demonstrated by Radomsky and Thole (2000). The difference in the accumulation of the oil film upstream of the saddle point, however, cannot be observed in Method 2. Instead, the accumulated mixture is spread widely in both upstream and downstream areas around the saddle point as in Fig. 6 and Fig. 8, and seems to bisect with respect to the separation line.

In Fig. 9, the endwall flow boundaries in the low turbulence case are compared to those in the high turbulence case. Here, no noticeable difference can be seen in the attachment line. On the other hand, the separation line as well as the boundary surrounding the suction-side corner vortex is remarkably altered under high free-stream turbulence. It can be expected that the inlet high free-stream turbulence and its thinning effect on the inlet momentum thickness tend to delay the endwall boundary-layer separation. By imposing the high free-stream turbulence, the point B_{L1} shifts downstream toward the point B_{H1} as expected, while surprisingly, the point B_{L2} moves toward the point B_{H2} contrary to the expectation. In addition, there is no major change in the central portion of the separation line regardless of the free-stream turbulence level, and the locations of the saddle points, S_L and S_H, are nearly identical to each other. As a result, in the presence of the high free-stream turbulence, the separation line from the point B_{L1} to S_L advances farther downstream, meanwhile that from the point S_L to B_{L2}, particularly near the endpoint B_{L2}, retreats. It is inevitable that the separation line between the points B_{L1} and S_L is confronted directly with the incoming near-wall flow, so that the flow separation along the line B_{L1}-S_L is liable to be delayed under high free-stream turbulence. As a result of the movement of the point B_{L1} toward B_{H1}, the point B_{L2} on the same blade is forced to move toward the point B_{H2}. This is because the incoming flow rushing toward the suction surface without separation should maintain a mass balance in the region upstream of the adjacent separation lines. It is noted that the distance along the suction-side corner between the points B_{L1} and B_{L2} on the same blade is approximately the same as that between the points B_{H1} and B_{H2}. As can be seen in Fig. 5, Fig. 7 and Fig. 9, the incoming

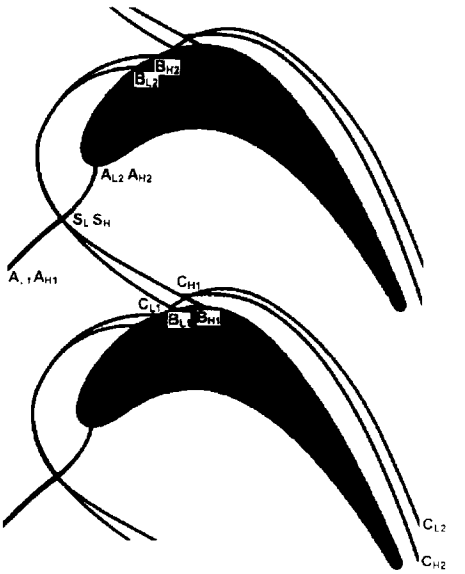

Fig. 9 Comparison of endwall flow boundaries between the low and high turbulence cases

near-wall flow between the adjacent separation lines in the high turbulence case collides with the suction surface more obliquely than that in the low turbulence case, which results in a lower upwash momentum, but delivers a higher axial momentum parallel with the endwall. Accordingly, less oil-film mixture climbs onto the suction surface under high free-stream turbulence. This is the reason why the point C_{H1} is located away from the suction-side corner, in contrast to the position of the point C_{L1}.

3.2 Baseline local heat/mass transfer data in the low turbulence case

The baseline distribution of St_m in the low turbulence case is shown in Fig. 10. The dotted lines in this figure indicate the flow boundaries found in Fig. 5. For clarity, the contours of St_m are drawn with an interval of 0.2×10^{-3} when $St_m<2.6\times10^{-3}$ and with an interval of 0.4×10^{-3} when $St_m>2.6\times10^{-3}$. In the low turbulence case, St_m value lies between $St_m=0.89\times10^{-3}$ and 5.59×10^{-3}. Based on the baseline local mass transfer distribution, the endwall surface is classified into seven different regions from Region A to Region G. Relatively low St_m is found in Region A at the entrance of the turbine passage, because the incoming boundary layer still extends in this area without any disturbances by the blade leading edge. Near the leading edge, there is a higher mass transfer region, Region B, which has the pressure- and suction-side wings designated by the long and short arrows, respectively. The long pressure-side wing extends from the attachment line almost up to the suction side of the neighboring blade across the turbine passage, nearly in parallel with the separation line. The long arrow is equivalent to the locus of the pressure-side leg of the horseshoe vortex. Contrary to the pressure-side wing, the suction-side wing has a very small area on the opposite side with respect to the attachment line, and it is resulted from the suction-side leg of the horseshoe vortex. A maximum of St_m value occurs at the corner of the leading edge, which is higher than 5.4×10^{-3}. This severe heat load is attributed to the existence of the leading-edge corner vortices. Region C is situated near the area where the incoming boundary-layer flow without separation meets the suction surface. The near-wall flow rushing toward the suction surface in the region upstream of the neighboring separation lines interacts strongly with it in Region C, resulting in a considerable flow disturbance. Consequently, the local mass transfer in Region C is fairly enhanced. There exists a pressure-side corner vortex along the corner between the endwall and the pressure surface. Higher mass transfer observed in Region D is resulted from the presence of the pressure-side corner vortex. Region E is in the form of a long strip along the suction-side corner. In Region E, there is a very steep gradient of St_m as well as a relatively high value of St_m. This region is equivalent mostly to the area bounded by the line C_{L1}-C_{L2} in Fig. 5, where the suction-side corner vortex is located. Figure 10 also shows that the suction-side corner vortex delivers higher mass transfer than the pressure-side one with a broader residing area. All over the endwall surface, the lowest mass transfer is found in Region F. Its boundary facing the suction surface corresponds nearly to the line C_{L1}-C_{L2}. The value of St_m in Region F is as low as about 1.0×10^{-3}, which is

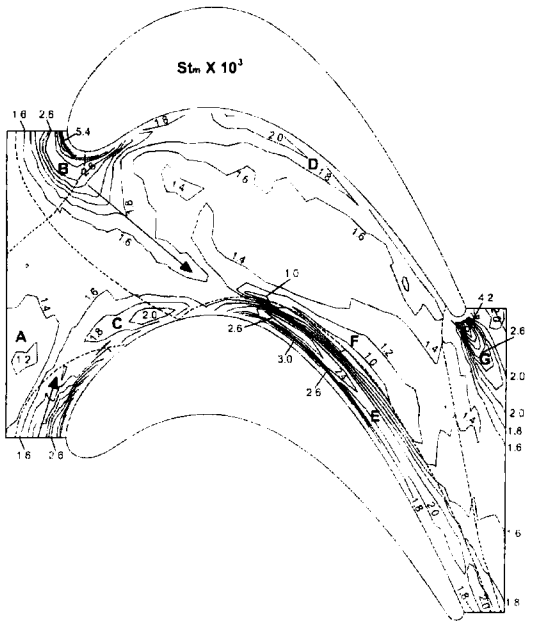

Fig. 10 Contours of St_m in the low turbulence case

about one fifth of the highest value of St_m in Region B. Severe local mass transfer is also found just behind the trailing edge (Region G). In this wake region, there exists an unsteady periodic vortex shedding, which greatly enhances the local mass transfer.

The variations of St_m along constant J lines are introduced in Fig. 11. The "J" stands for the J-th measurement locations in the pitchwise direction as indicated in Fig. 4. Thus, "J=1" and "J=21" mean the suction- and pressure-side boundaries of the measurement area, respectively. As noted earlier, the two boundaries are positioned about 2mm apart from the blade-endwall corner within the cascade passage. The values of St_m for "J=1" and "J=21" have nearly the same values along the upstream and downstream symmetry lines. Therefore, the measured mass transfer data have a good pitchwise periodicity at both inlet and exit of the cascade. Along the pressure-side boundary (J=21), St_m rapidly increases and has a maximum value of 5.59×10^{-3} at $x/b=-0.00625$. After passing this peak, St_m sharply decreases to the value of about 1.62×10^{-3} at $x/b=0.25$. Then, St_m increases and shows another peak of 2.24×10^{-3} at $x/b=0.4$. This increase is related closely to the pressure-side corner vortex. A sharp spike is found near the exit of the cascade passage. The sharp peak, situated on the centerline of the wake, has its value of $St_m=3.93\times10^{-3}$ that is less than the maximum value in Region B. Along the suction-side boundary (J=1), St_m also rapidly increases at the inlet of the cascade passage, and then sharply decrease. A closer observation shows the existence of the second peak of $St_m=1.89\times10^{-3}$ at $x/b=0.25$. This lower peak is located in Region C, as discussed in Fig. 10. At $x/b=0.5$, there is a third peak of St_m and its value reaches 3.21×10^{-3}. Higher mass transfer at this location arises from the suction-side corner vortex in Region E (Fig. 10). Along the line of J=7, there is a deep valley where $St_m=0.89\times10^{-3}$ at $x/b=0.75$. This minimum value is found to be the lowest value all over the endwall measurement area. This location is situated in Region F in Fig. 10.

Local pitchwise variations of St_m along constant I line are presented in Fig. 12. The length, l, denotes the pitchwise distance between the pressure and suction surfaces along each constant I line, and ys stands for the distance from the suction surface along each constant I line. At $x/b=0.25$, St_m has two noticeable peaks at $y_s/l=0.049$, and 0.909 in Region C and in an area occupied by the pressure-side leading-edge corner vortex, respectively. At $x/b=0.50$, St_m has two local minimums at ys/l=0.054 and 0.143 as well as three local maximums near the suction surface, at around $y_s/l=0.083$, and near the pressure surface. In addition, there exists a very steep gradient of St_m in the y_s-direction near the suction surface. The third local maximum near the pressure surface results from the pressure-side

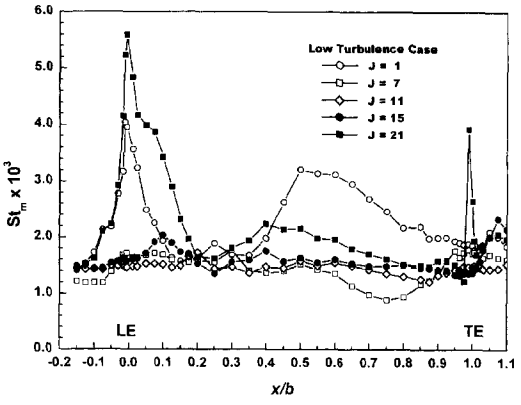

Fig. 11 Profiles of St_m along constant J lines in the low turbulence case

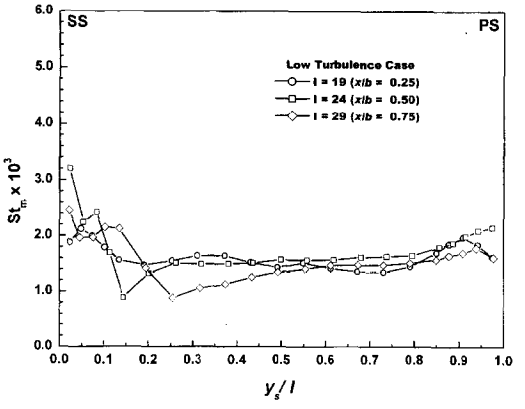

Fig. 12 Profiles of St_m along constant I lines in the low turbulence case

corner vortex. At $x/b=0.75$, the trend of St_m at $x/b=0.5$ is still maintained, but the locations of the second local minimum and maximum shift toward the center of the cascade passage along with a milder gradient of St_m. In addition, due to the downstream development of the pressure-side corner vortex, the third local maximum near the pressure surface shifts away from it. The minimum values of St_m at $x/b=0.5$ and 0.75 belong to Region F in Fig. 10.

The previous mass transfer work for a rotor blade in the low turbulence case (Goldstein and Spores, 1988) provided very similar results in comparison with that in Fig. 10, even if their Reynolds number is about half of ours. They confirmed the existence of Region A through Region G as classified in this study. The only noticeable qualitative difference between the two studies is that a very long pressure-side wing of Region B is observed in this study. This difference might originate from the present lower pitch-to-chord ratio and thicker momentum thickness. However, there are still considerable discrepancies in recent heat transfer investigations even in the low free-stream turbulence case. The heat transfer measurement for a rotor cascade by Giel et al.(1998) showed the existence of Region A, Region B, Region E and Region G, but they could not provide any evidences of two wings in Region B, Region C, Region D, and Region F. For a stator vane, Kang et al.(1999) showed totally different tendencies. They could not find two wings in Region B, Region C, Region F and Region G. Moreover, even Region D and Region E were not clearly seen in their results. Instead, they showed a relatively steep gradient of the heat transfer Stanton number in the axial direction, with a lower heat transfer value in the central region of the passage.

3.3 Local heat/mass transfer in the high turbulence case

Figure 13 shows the local mass transfer Stanton number contours in the high turbulence case. In this case, St_m has its value in the range from about 1.62×10^{-3} to 5.8×10^{-3}. The minimum value of St_m is about two times higher than that in the low turbulence case, but the maximum values in both cases are roughly the same. The overall mass transfer distributions in Fig. 10 and Fig. 13 show a similar qualitative trend regardless of the free-stream turbulence level. Under high turbulence, however, the regions classified as A to G in Fig. 10 tend to lose their identities except for the Region B, Region C and Region G. It is noted that St_m in the central region of the turbine passage in the high turbulence case has a fairly higher value than that in the low turbulence case. As a result of an intense lateral turbulent mixing, relatively low St_m in Region A of Fig. 10 is hardly found at the entrance in Fig. 13. Under high free-stream turbulence, the most active mass transfer is still observed near the leading-edge corner, but the pressure- and suction-side wings in Region B in Fig. 10 cannot be identified in Fig. 13. In particular, the pressure-side wing experiences a dramatic change. In the high turbulence case, higher mass transfer is still found in Region C. There is a slightly milder gradient of St_m along the pressure-side corner in Region D of Fig. 13 in comparison with that in Fig. 10. The most notable changes in the mass transfer distribution due to the high turbulence are seen along the suction-side corner, that is, both in Region E and Region F. A much milder gradient of St_m can be seen as well as a lower peak value of St_m near the suction-side corner compared to those in Fig. 10. Under high free-stream turbulence, the mass transfer in Region F suffers a considerable augmentation, so that the steep gradient of St_m between Region E and F in Fig. 10 almost disappears. The lowest values of St_m all over the measurement area are always found in Region F, and it increases from 0.89×10^{-3} to 1.62×10^{-3} with increasing free-stream turbulence. These changes in mass transfer in Region E and Region F are related closely to the fact that the region bounded by the line C_{L1}-C_{L2} in Fig. 5 undergoes a considerable reduction in its width under high free-stream turbulence. As in the low turbulence case, the higher mass transfer region near the suction-side corner in Fig. 13 coincides approximately with the region surrounded by the line C_{H1}-C_{H2}. In Fig. 13, higher mass transfer is also

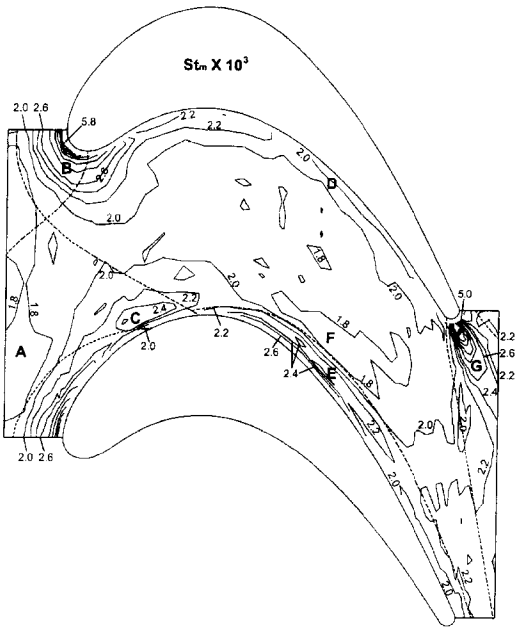

Fig. 13 Contours of St_m in the high turbulence case

found in the wake region behind the trailing edge, and its peak value is higher than that in Fig. 10. The St_m value in the endwall region other than Region A to Region G is in the range roughly between $St_m=1.4\times10^{-3}$ to 1.6×10^{-3} in the low turbulence case, meanwhile it varies approximately from $St_m=1.8\times10^{-3}$ to 2.0×10^{-3} in the high turbulence case.

Downstream distributions of St_m along constant J lines are shown in Fig. 14 in the high turbulence case. In comparison with the data in Fig. 11, the variation of St_m is not significant along the constant J lines, but local mass transfer is certainly enhanced. The St_m near the leading edge along the pressure- and suction-side boundaries has its peak values of $St_m=5.81\times10^{-3}$ and 4.89×10^{-3}, respectively, and the St_m near the trailing edge along the J=21 line has a peak value of 4.51×10^{-3}. A direct comparison of these peak values with those in Fig. 11 shows that the relative increments in their magnitudes are very small. However, the relative increments of St_m along the lines of J=7, 11, and 15 are much larger. In Fig. 14, the second peak can be seen at $x/b=0.4$ along the pressure-side boundary, which supports the existence of the pressure-side corner vortex in

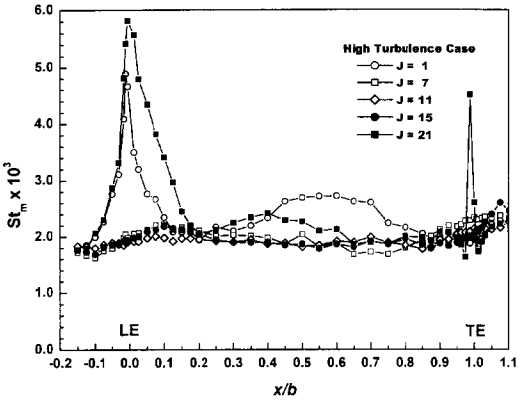

Fig. 14 Profiles of St_m along constant J lines in the high turbulence case

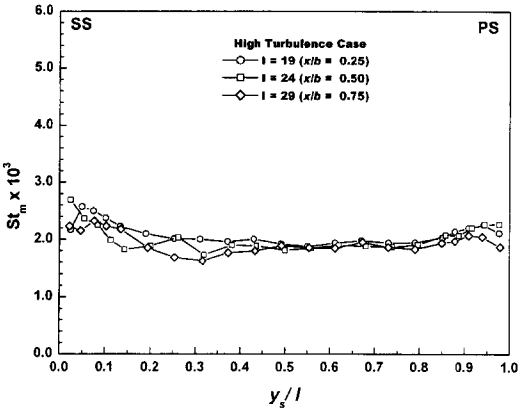

Fig. 15 Profiles of St_m along constant I lines in the high turbulence case

Region D even in the high turbulence case. Along the suction-side boundary, there is the second tiny peak at $x/b=0.25$ in Region C and the third blunt peak at $x/b=0.6$ in Region E. Along the line J=7, there is a significant increase in St_m in Region F between $x/b=0.6$ and 0.9, compared to the result in Fig. 11.

Local pitchwise variations of St_m along the constant I line in the high turbulence case are presented in Fig. 15. In general, the St_m in the high turbulence case has a higher value, compared with that in Fig. 12, and regardless of x/b, there is a minute pitchwise variation in St_m even near the suction surface. At $x/b=0.50$ in Fig. 12, St_m has two local maximums and minimums with a steep gradient near the suction surface. At $x/$

b=0.50 in the high turbulence case, however, St_m decreases monotonically without any steep gradient departing from the suction surface. At x/b= 0.5, the maximum value of St_m near y_s/l=0.0 decreases from about 3.21×10^{-3} (Fig. 12) to 2.69×10^{-3} (Fig. 15), meanwhile the minimum value found at y_s/l=0.143 increases twofold from 0.89×10^{-3} to 1.82×10^{-3}. Due to this rapid increase in the minimum value, it is not easy to identify Region F in the high turbulence case.

In this study for a turbine rotor cascade, the high free-stream turbulence enhances the heat/mass transfer in the central area of the turbine passage, but only a slight augmentation is found in the endwall regions adjacent to the leading and trailing edges. Therefore, the high free-stream turbulence makes the endwall heat load more uniform. The endwall surface is classified into the seven different regions based on the local heat/mass transfer distribution, and the effects of high free-stream turbulence on local heat/mass transfer in each region are discussed in detail. Radomsky and Thole (2000) for a stator vane also concluded that while the high free-stream turbulence increases the endwall heat transfer, low augmentations are found to coincide with the region having the most intense vortex motions. However, the two results show quite different local distributions. Their data in the high turbulence case could not identify at least Region C, Region F, and Region G.

3.4 Average heat/mass transfer

The mass transfer Stanton number averaged in the pitchwise or y-direction, $\overline{St}_m$, is introduced in Fig. 16. The average Stanton number steeply increases in the upstream region of the cascade and has a sharp peak at the inlet. At the exit of the cascade, there is another increase in $\overline{St}_m$. This tendency is observed independent of the free-stream turbulence level. The mass transfer Stanton number averaged across the whole measurement area, $(\overline{St}_m)_{av}$, is evaluated to be 1.69×10^{-3} in the low turbulence case and 2.15×10^{-3} in the high turbulence case. In other words, the elevated free-stream turbulence results in about 27 percent enhancement in the mass transfer. A repeatability

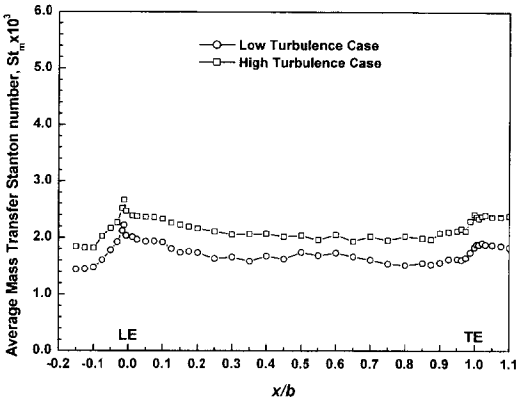

Fig. 16 Profiles of pitch-wise averaged mass transfer Stanton number, $\overline{St}_m$

test in the present low turbulence case shows that the deviation of $(\overline{St}_m)_{av}$ is only within 0.59%. As mentioned earlier, the average mass transfer is augmented by about 6 percent as a result of the thinner momentum thickness in the high turbulence case. Radomsky and Thole (2000) reported that for most of the axial distance, the augmentation due to their high free-stream turbulence is relatively constant at 25 percent above their low turbulence case. In their study, the difference in momentum thickness between the two cases resulted in a 9.5 percent augmentation in the high turbulence case. Thus, in the viewpoint of averaged quantity, the present result is in a good agreement with that by Radomsky and Thole (2000) in the convective transport augmentation, although the two results show quite different local distributions.

4. Conclusion

The effects of a combustor-level high free-stream turbulence on the endwall convective transport have been investigated for a linear high-turning turbine rotor cascade, by employing the partial- and full-coverage oil-film visualizations and the naphthalene sublimation technique.

(1) The endwall oil-film flow visualizations show that the high free-stream turbulence has little effect on the attachment line, but alters the separation line noticeably. Due to downstream

shifts of the separation line at both ends, the incoming near-wall flow upstream of the adjacent separation lines in the high turbulence case collides more obliquely with the suction surface than that in the low turbulence case. A weaker lift-up force arising from this more oblique collision results in the narrower suction-side corner vortex area in the high turbulence case.

(2) The high free-stream turbulence enhances the heat/mass transfer in the central area of the turbine passage, but only a slight augmentation is found in the endwall regions adjacent to the leading and trailing edges. Therefore, the high free-stream turbulence makes the endwall heat load more uniform.

(3) Regardless of the free-stream turbulence level, severe heat loads are always found in the areas occupied by the leading-edge corner vortices and the trailing-edge vortex shedding. The heat/mass transfers along the locus of the pressure-side leg of the leading-edge horseshoe vortex and along the suction-side corner are influenced most strongly by the high free-stream turbulence.

(4) In this study, the endwall surface is classified into seven different regions based on the local heat/mass transfer distribution, and the high turbulence effects on local heat/mass transfer in each region are discussed in detail.

(5) The average heat/mass transfer coefficient across the entire endwall region is enhanced by 27 percent under the high free-stream turbulence.

References

Abernethy, R. B., Benedict, R. P., and Dowdell, R. B., 1985, "ASME Measurement Uncertainty," *ASME Journal of Fluids Engineering*, Vol. 107, pp. 161~164.

Blair, M. F., 1974, "An Experimental Study of Heat Transfer and Film Cooling on Large-Scale Turbine Endwalls," *ASME Journal of Heat Transfer*, Vol. 96, pp. 524~529.

Camp, T. R., and Shin, H.-W., 1995, "Turbulent Intensity and Length Scale Measurements in Multistage Compressors," *ASME Journal of Turbomachinery*, Vol. 117, pp. 38~46.

Gaugler, R. E., and Russell, L. M., 1984, "Comparison of Visualized Turbine Endwall Secondary Flows and Measured Heat Transfer Pattern," *ASME Journal of Engineering for Gas Turbine and Power*, Vol. 106, pp. 168~172.

Giel, P. W., Thurman, D. R., Fossen, G. J. V., Hippensteele, S. A., and Boyle, R. J., 1998, "Endwall Heat Transfer Measurements in a Transonic Turbine Cascade," *ASME Journal of Turbomachinery*, Vol. 120, pp. 305~313.

Goebel, S. G., Abuaf, N., Lovett, J. A., and Lee C. P., 1993, "Measurements of Combustor Velocity and Turbulence Profile," ASME Paper No. 93-GT-228.

Goldstein, R. J., Lau, K. Y., and Leung, C. C., 1983, "Velocity and Turbulence Measurements in Combustion System," *Experiments in Fluids*, Vol. 1, pp. 93~99.

Goldstein, R. J., and Spores, R. A., 1988, "Turbulent Transport on the Endwall in the Region Between Adjacent Turbine Blades," *ASME Journal of Heat Transfer*, Vol. 110, pp. 862~869.

Goldstein, R. J., and Cho, H. H., 1995, "A Review of Mass Transfer Measurements Using Naphthalene Sublimation," *Experimental Thermal and Fluid Science*, Vol. 10, pp. 416~434.

Graziani, R. A., Blair, M. F., Taylor, J. R., and Mayle, R. E., 1980. "An Experimental Study of Endwall and Airfoil Surface Heat Transfer in a Large Scale Turbine Blade Cascade," *ASME Journal of Engineering for Power*, Vol. 102, pp. 257~267.

Hudson, H. P. and Dominy, R. G., 1987, Three -Dimensional Flow in a Low-Pressure Turbine Cascade at Its Design Condition," *ASME Journal of Engineering for Power*, Vol. 109, pp. 177~185.

Jun, S. B., 2000, Measurements of Endwall Heat (Mass) Transfer Coefficient in a Linear Turbine Cascade Using Naphthalene Sublimation Technique, MS thesis, Kumoh National Institute of Technology.

Kang, M. K. B., Kohli, A., and Thole, K. A., 1999, "Heat Transfer and Flowfield Measurements in the Leading Edge Region of a Stator Vane Endwall," *ASME Journal of Turbomachinery*, Vol. 121, pp. 558~568.

Kang, M. K. B., and Thole, K. A., 2000, "Flow-field Measurements in the Endwall Region of a Stator Vane," *ASME Journal of Turbomachinery*, Vol. 122, pp. 458~466.

Koutmos, P. and McGuirk, J. J., 1989, "Isothermal Flow in a Gas Turbine Combustor-A Benchmark Experimental Study," *Experiments in Fluids*, Vol. 7, pp. 344~354.

Lee, S. W., Kim, Y. B., and Lee, J. S., 1997, "Flow Characteristics and Aerodynamic Losses of Film-Cooling Jets With Compound Angle Orientation," *ASME Journal of Turbomachinery*, Vol. 119, pp. 310~319.

Oke, R. A., Burd, S. W., Simmon, T. W., and Vahlberg, R., 2000, "Measurements in a Turbine Cascade over a Contoured Endwall: Discrete Hole Injection of Bleed Flow," ASME Paper No. 2000-GT-214.

Radomsky, R. W., and Thole, K. A., 2000, "High Free-Stream Turbulence Effects on Endwall Heat Transfer for a Gas Turbine Stator Vane," *ASME Journal of Turbomachinery*, Vol. 122, pp. 699~708.

Spencer, M. C., Jones, T. V., and Lock, G. D., 1996, "Endwall Heat Transfer Measurements in an Annular Cascade of Nozzle Guide Vanes at Engine Representative Reynolds number and Mach numbers," *International Journal of Heat and Fluid Flow*, Vol. 17, pp. 139~147.

STP 470A, 1974, Manual on the Use of Thermocouples in Temperature Measurement, published by ASTM.

Wang, H. P., Goldstein, R. J., and Olson, S. J., 1999, "Effect of High Free-Stream Turbulence With Large Length Scale on Blade Heat/Mass Transfer," *ASME Journal of Turbomachinery*, Vol. 121, pp. 217~224.

York, R. E., Hylton, L. D., and Mihelc, M. S., 1984, "An Experimental Investigation of Endwall Heat Transfer and Aerodynamics in a Linear Vane Cascade," *ASME Journal of Engineering for Gas turbine and power*, Vol. 106, pp. 159~167.